

# Optimization study of third harmonic generation in quantum cascade lasers

Ali Mojibpour,<sup>1</sup> Mahdi Pourfath,<sup>1,2,\*</sup> and Hans Kosina<sup>2</sup>

<sup>1</sup> School of Electrical and Computer Engineering, University of Tehran, Tehran, Iran

<sup>2</sup> Institute for Microelectronics, TU Wien, Gußhausstraße 27-29/E360, 1040 Vienna, Austria

\*[pourfath@ut.ac.ir](mailto:pourfath@ut.ac.ir)

**Abstract:** A systematic optimization study of quantum cascade lasers with integrated nonlinearity for third-harmonic generation is performed. To model current transport the Pauli master equation is solved using a Monte Carlo approach. A multi-objective particle swarm optimization algorithm is applied to obtain the Pareto front. Our theoretical analysis indicates an optimized structure with five orders of magnitude increase in the generated third-harmonic power with respect to the reference design. This striking performance comes with a low threshold current density of about 1.6 kA/cm<sup>2</sup> and is attributed to double resonant phonon scattering assisted extraction and injection scheme of the laser.

© 2014 Optical Society of America

**OCIS codes:** (190.2620) Harmonic generation and mixing; (140.3070) Infrared and far-infrared lasers; (140.5965) Semiconductor lasers, quantum cascade.

---

## References and links

1. N. Owschikow, C. Gmachl, A. Belyanin, V. Kocharovskiy, D. L. Sivco, R. Colombelli, F. Capasso, and A. Y. Cho, "Resonant second-order nonlinear optical processes in quantum cascade lasers," *Phys. Rev. Lett.* **90**, 043902 (2003).
2. M. Jang, R. Adams, J. Chen, W. Charles, C. Gmachl, L. Cheng, F.-S. Choa, and M. Belkin, "Room-temperature operation of 3.6  $\mu\text{m}$  InGaAs/AlInAs quantum cascade laser sources based on intracavity second harmonic generation," *Appl. Phys. Lett.* **97**, 141103 (2010).
3. M. A. Belkin, F. Capasso, F. Xie, A. Belyanin, M. Fischer, A. Wittmann, and J. Faist, "Room temperature terahertz quantum cascade laser source based on intracavity difference-frequency generation," *Appl. Phys. Lett.* **92**, 201101–201101 (2008).
4. A. Bismuto, R. Terazzi, B. Hinkov, M. Beck, and J. Faist, "Fully automatized quantum cascade laser design by genetic optimization," *Appl. Phys. Lett.* **101**, 021103–021103 (2012).
5. H. Callebaut and Q. Hu, "Importance of coherence for electron transport in terahertz quantum cascade lasers," *J. Appl. Phys.* **98**, 104505 (2005).
6. P. Q. Liu, A. J. Hoffman, M. D. Escarra, K. J. Franz, J. B. Khurgin, Y. Dikmelik, X. Wang, J.-Y. Fan, and C. F. Gmachl, "Highly power-efficient quantum cascade lasers," *Nat. Photonics* **4**, 95–98 (2010).
7. M. A. Belkin, F. Capasso, A. Belyanin, D. L. Sivco, A. Y. Cho, D. C. Oakley, C. J. Vineis, and G. W. Turner, "Terahertz quantum-cascade-laser source based on intracavity difference-frequency generation," *Nat. Photonics* **1**, 288–292 (2007).
8. R. W. Boyd, *Nonlinear Optics* (Academic, 2008), 3rd ed.
9. M. V. Fischetti, "Master-equation approach to the study of electronic transport in small semiconductor devices," *Phys. Rev. B* **59**, 4901 (1999).
10. G. Milovanovic and H. Kosina, "A semiclassical transport model for quantum cascade lasers based on the Pauli master equation," *J. Comput. Electron.* **9**, 211–217 (2010).
11. C. Sirtori, F. Capasso, J. Faist, and S. Scandolo, "Nonparabolicity and a sum rule associated with bound-to-bound and bound-to-continuum intersubband transitions in quantum wells," *Phys. Rev. B* **50**, 8663 (1994).
12. A. Yariv, *Quantum Electronics* (Wiley, 1988), 3rd ed.
13. T. Mosely, A. Belyanin, C. Gmachl, D. Sivco, M. Peabody, and A. Cho, "Third harmonic generation in a quantum cascade laser with monolithically integrated resonant optical nonlinearity," *Opt. Express* **12**, 2972–2976 (2004).

14. C. Jirauschek, "Monte Carlo study of carrier-light coupling in terahertz quantum cascade lasers," *Appl. Phys. Lett.* **96**, 011103 (2010).
15. J. Faist, D. Hofstetter, M. Beck, T. Aellen, M. Rochat, and S. Blaser, "Bound-to-continuum and two-phonon resonance, quantum-cascade lasers for high duty cycle, high-temperature operation," *IEEE J. Quantum Elect.* **38**, 533–546 (2002).
16. D. Hofstetter, M. Beck, T. Aellen, and J. Faist, "High-temperature operation of distributed feedback quantum-cascade lasers at  $5.3\ \mu\text{m}$ ," *Appl. Phys. Lett.* **78**, 396–398 (2001).
17. Q. J. Wang, C. Pflugl, L. Diehl, F. Capasso, T. Edamura, S. Furuta, M. Yamanishi, and H. Kan, "High performance quantum cascade lasers based on three-phonon-resonance design," *Appl. Phys. Lett.* **94**, 011103–011103 (2009).
18. M. Yamanishi, K. Fujita, T. Edamura, and H. Kan, "Indirect pump scheme for quantum cascade lasers: dynamics of electron-transport and very high  $T_0$ -values," *Opt. Express* **16**, 20748–20758 (2008).
19. S. Kumar, C. W. I. Chan, Q. Hu, and J. L. Reno, "A 1.8-thz quantum cascade laser operating significantly above the temperature of  $\hbar\omega/k_B$ ," *Nature Physics* **7**, 166–171 (2011).
20. D. Botez, S. Kumar, J. Shin, L. Mawst, I. Vurgaftman, and J. Meyer, "Temperature dependence of the key electro-optical characteristics for midinfrared emitting quantum cascade lasers," *Appl. Phys. Lett.* **97**, 071101 (2010).
21. A. Wacker, "Extraction-controlled quantum cascade lasers," *Appl. Phys. Lett.* **97**, 081105 (2010).
22. J. Faist, "Wallplug efficiency of quantum cascade lasers: Critical parameters and fundamental limits," *Appl. Phys. Lett.* **90**, 253512–253512 (2007).

## 1. Introduction

Since their first successful demonstration in 1994, quantum cascade lasers (QCLs) have matured and dominated mid-infrared (mid-IR) applications. Due to their unique design flexibility, an efficient intra-cavity wavelength conversion method based on the incorporation of a nonlinear material into the pump QCL has been proposed [1]. Extensive efforts have been undertaken in employing intra-cavity wavelength conversion in the near [2] and far-IR [3] range. The performance of a QCL depends on various parameters, such as the electronic and optical properties of the base material, layer thicknesses, the applied electric field, and temperature. Because of this huge parameter space, a variety of designs have been proposed. Until recently [4], no systematic optimization of a QCL has been performed. This work presents a systematic multi-objective particle swarm optimization of layer thicknesses and electric field of QCLs for third harmonic generation (THG) at room temperature. Doping density is fixed to  $2.5 \times 10^{16}\text{cm}^{-3}$  in the optimization process [Fig. 1(a)], but as discussed later all the subsequent figures and discussions are based on a doping density of  $7.5 \times 10^{16}\text{cm}^{-3}$  for both the reference and optimized design.

## 2. Approach

The fact that the achieved optimum points may lie in the region where the underlying model fails, i.e., region corresponding to designs with unphysical electron coherence length [4], can make systematic optimization useless. In this work, however, such pathological structures are avoided in the optimization process. The results indicate that a large threshold optical gain ( $35\text{ cm}^{-1}$  for a laser with an injector doping level of  $2.5 \times 10^{16}\text{ cm}^{-3}$ ), drives the optimization to structures with physical electron coherence length. Electron's coherence length, the length over which electron is described by a single coherent wave packet, is equivalent to the length the wavefunction extends to. Hence the search for structures with small electron coherent length is the search for structures with strongly confined basis states. When the module length ( $L_{\text{mod}}$ ) is relatively small, similar to the 14-layer structure considered in this work, every single state plays an important role and the following argument justifies our approach. Large optical gain is always accompanied with efficient depletion and selective injection of electrons from the lower lasing level ( $l$ ) to the upper lasing level ( $u$ ). These features cannot come together in structures containing weakly confined states. In general, three kinds of structures can be specified: (1) structures with both strongly and weakly confined states, (2) structures consist of only weakly confined states, and (3) structures with only strongly confined states. Case (2) disfavors the

selectivity of injection to level  $u$ , specially for structures with relatively small  $L_{\text{mod}}$ . Selectivity of injection is crucial for establishing population inversion and it was to this end that injector barrier was introduced to QCL designs. Case (1) suffers not only from a lower selectivity of injection caused by those weakly confined states, but also from a slower depletion of  $l$ . Depletion of  $l$  in all design schemes of QCL occurs through scattering. A large scattering rate, needed for fast depletion of  $l$ , requires large overlap between the initial and the final states. The overlap integral of a weakly and a strongly confined state cannot be large. Therefore, the scattering rate for case (1) is relatively small and the depletion of electrons from  $l$  is rather slow. Only case (3) can have the best depletion efficiency and injection selectivity at the same time and hence, very large optical gain. The condition of a sufficiently large threshold optical gain, therefore corresponds to a part of the search space where the structures are mostly of the type of case (3) and the optimization process chooses the best these structures. The localization of wavefunction due to dephasing scattering, which occurs for thick barriers with small anticrossing gap [5], is not addressed here. However, such cases are favorite only for far-IR QCL designs and several execution of the optimization process shows no convergence to such pathological structures (i.e., structure containing thick barriers with small anticrossing). It should be noted that the injector barrier thickness, known as the bottleneck of most designs [6], can go under systematic optimization with this technique.

The merit function for THG in QCLs is defined based on the third-harmonic (TH) power which, in the slowly varying envelope approximation [7], is

$$W_{3\omega} = \frac{9\omega^2}{16c^4 \epsilon_0^2 n_{\text{eff}}^2(3\omega) n_{\text{eff}}^3(\omega)} \frac{|\chi^{(3)}(3\omega)|^2}{S_{\text{eff}}} W_{\omega}^3 l_{\text{coh}}^2, \quad (1)$$

where  $S_{\text{eff}}$  is the effective interaction area,  $l_{\text{coh}} = (|k_{3\omega} - 3k_{\omega}|^2 + (\alpha/2)^2)^{-1/2}$  is the coherence length, and  $\alpha$  is the loss at the TH frequency.  $\omega$ ,  $n_{\text{eff}}(\omega)$ , and  $W_{\omega}$  are the fundamental frequency, the effective refractive index, and the power at frequency  $\omega$ , respectively.  $\chi^{(3)}(3\omega)$  is the third-order susceptibility [8]. Merit function is defined as  $|\chi^{(3)}(3\omega)|^2 W_{\omega}^3$ .

Pauli master equation is used to model charge transport [9]. A Monte Carlo approach is used to solve the transport equation [10]. Band nonparabolicity effects are taken into account by employing an effective two-band  $\mathbf{k} \cdot \mathbf{p}$  model [11]. Important scattering mechanisms, such as polar longitudinal optical phonon ( $\hbar\omega_{\text{LO}} = 33\text{meV}$ ), interface roughness (mean height  $\Delta = 12\text{\AA}$  and correlation length  $\Gamma = 90\text{\AA}$ ), alloy scattering (alloy scattering potential  $U = 360\text{meV}$ ), and acoustic phonon scattering ( $\Xi = 8\text{eV}$ ) are considered. To estimate the intra-cavity power, a rate equation description of the active region and injector is utilized. Assuming negligible degeneracy difference between  $l$  and  $u$ , the intra-cavity power reads as [12]

$$W_{\omega} = \frac{8\pi n_{\text{eff}}(\omega) \hbar c A_m L t_{\text{spon}}}{3g(v_0) \lambda^3 \tau} \left( g_0 - \frac{\alpha_w + \alpha_m}{\Gamma} \right), \quad (2)$$

where  $g(v_0)$  is the value of normalized line-shape function at the lasing frequency,  $\tau = t_3(1 + (1 - (t_3/t_{32}))t_2/t_3)$  with  $t_3$  and  $t_2$  representing the lifetime of  $u$  and  $l$ , respectively, and  $t_{32}$  is the relaxation time from  $u$  to  $l$ .  $A_m$ ,  $g_0$ ,  $\Gamma$ ,  $\alpha_w$ ,  $\alpha_m$ ,  $L$  and  $t_{\text{spon}}$  are the mode cross-section, optical gain, confinement factor, waveguide loss, mirror loss, cavity length, and spontaneous emission lifetime, respectively. This non-selfconsistent approach significantly reduces computation time. The structure described in [13] is considered as the reference design. Based on the reported parameters, our model predicts that the merit function for THG peaks at an electric field of 46.5 kV/cm which agrees well with the observed value of 42 kV/cm.

### 3. Results and discussion

The Pareto front, i.e., the set of non-dominated solutions, for THG is depicted in Fig. 1(a). All of the non-dominated solutions, indicated by circles in Fig. 1(a), have roughly the same TH power. Due to the higher linear-to-nonlinear power conversion efficiency  $\eta_{\text{NL}}$ , defined as  $\eta_{\text{NL}} = W_{3\omega}/W_{\omega}^3 \propto |\chi^{(3)}(3\omega)|^2$ , the solution with the second best THG performance is selected. Figure 1(b) compares the estimation of pump power obtained based on Eq. (2) with that of selfconsistent approach [14]. Figure 1(c) depicts the merit function and the pump wavelength as functions of the applied electric field. The merit function peaks at an electric field of 60.1 kV/cm. Figures 2(a) and 2(b) compare the reference and the optimized designs and Fig. 2(c) depicts a schematic of the optimized design. Two cascades 1-2-3-4 and 1-2-3-5 with the dipole matrix elements  $z_{12} = 11.3\text{\AA}$ ,  $z_{23} = 7.8\text{\AA}$ ,  $z_{34} = 38.6\text{\AA}$ ,  $z_{14} = 5.9\text{\AA}$ ,  $z_{35} = 7.6\text{\AA}$  and  $z_{15} = 3.2\text{\AA}$  have major contributions to  $\chi^{(3)}$ . Since the defined merit function favors the pump power, the third-order susceptibility of the optimized design is not as large as that of the reference design. The extra cascade (1-2-3-5) is responsible for the decrease of  $\chi^{(3)}$ . Since  $z_{35}$  and  $z_{15}$  are relatively small, this cascade does not strongly contribute to  $\chi^{(3)}$ , but due to the sum-rule for electronic intersubband transitions [11], the added state (state 5) reduces the possible dipole matrix elements of the other transitions. This results in 10-fold decrease in  $\chi^{(3)}$ . The layer sequence of the optimized structure for one period, in nanometers, starting with the intra-injector barrier, is: **3.1**/3.0/**2.3**/3.2/**2.2**/3.0/**3.0**/3.1/**2.1**/5.0/**2.3**/4.9/**1.6**/4.2 where  $\text{In}_{0.52}\text{Al}_{0.48}\text{As}$  barrier layers are shown in bold,  $\text{In}_{0.53}\text{Ga}_{0.47}\text{As}$  well layers are represented in roman, and n-doped layers ( $7.5 \times 10^{16} \text{ cm}^{-3}$ ) are underlined.

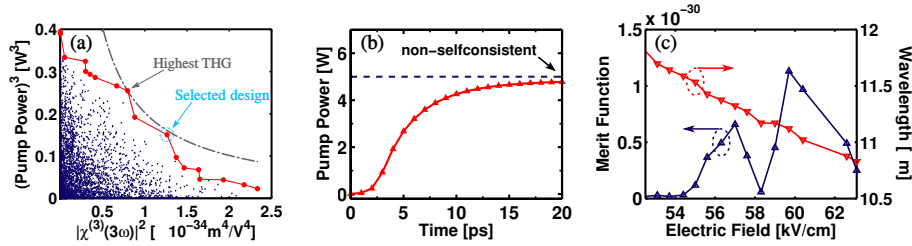


Fig. 1. (a) Pareto front for THG. Triangles represent the results of various particles in the search space and circles indicate the obtained Pareto front. The dash-dot line corresponds to the merit function of the best design if it had different values of  $\chi^{(3)}$ . (b) Temporal evolution of the intra-cavity power in the optimized device. The prediction of Eq. (2) is indicated by the dashed line. A typical mode cross-section of  $90\mu\text{m}^2$  is used in the calculations. Single-mode optical cavity is assumed. (c) The merit function and wavelength of the optimized design as functions of the applied electric field. Strong linear Stark tuning of the pump laser transition around the peak of the merit function allows a broad tunability of the generated TH frequency.

The reference design is based on single resonant phonon extraction. Resonant electron scattering by longitudinal optical (LO) phonons is the fastest intersubband relaxation process ( $\sim 0.2\text{ps}$ ) and can provide the most efficient extraction. However, relatively long tunneling times ( $\sim 2 - 4\text{ps}$ ) [15] reduce the overall extraction efficiency of this scheme. Such a bottleneck can increase the anticipated population ratio of the  $l$  and  $u$  states ( $\eta = n_l/n_u$ ) from 0.2 (based on the lifetimes  $\eta = \tau_l/\tau_{ul}$ ) to a value as large as 0.59 [15]. Double [16] and triple [17] resonant phonon extraction schemes have been proposed to facilitate extraction and limit the drawback of the long tunneling time to the injection/relaxation region. These schemes succeeded in reducing  $\eta$  to 0.35 and 0.22, respectively. For the reference structure  $\eta = 0.43$  which agrees with the expectation from single resonant phonon schemes. The proposed structure is based on

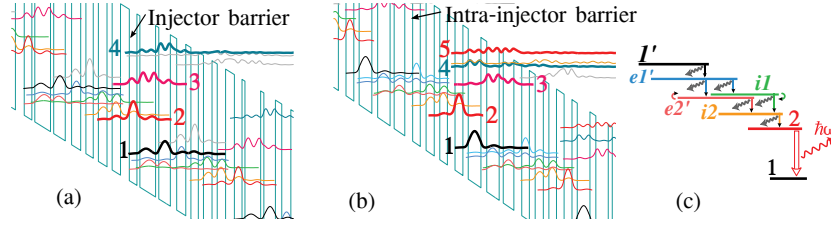


Fig. 2. Conduction band diagrams and squared wavefunctions of (a) the reference design at an electric field of 46.5 kV/cm. (b) The optimized design at an electric field of 60.1 kV/cm, where the merit function peaks. The optimized structure can be viewed as double phonon-photon-double phonon (5P) structure. (c) The schematic of the transition between levels of the optimized design. ‘e’ and ‘i’ represent the extractor and injector levels, respectively.

double resonant phonon extraction. However,  $\eta = 0.15$  even surpasses the value found in the triple resonant phonon extraction scheme. Furthermore, differential transition efficiencies of  $\eta_{tr} = 84\%$  at the largest merit function and of  $\eta_{tr} = 95\%$  near the threshold are superior to 58% efficiency of the triple resonant phonon QCL [17] at the maximum optical power despite the latter has 160% larger  $L_{mod}$ . Such a behavior can be attributed to the scattering-assisted injection scheme of the proposed design. Indirect pumping of electrons to an intermediate level separated

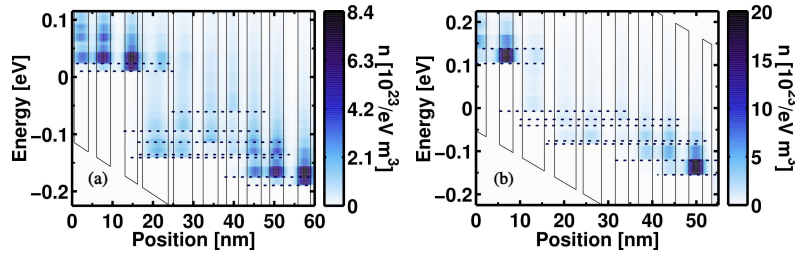


Fig. 3. Energy-position-resolved electron density of the (a) reference and (b) optimized design at  $T = 300\text{K}$  and at the electric field of maximum merit function.

by the LO phonon energy from level  $u$  [18] has already shown remarkable results [19]. The distinguished feature of indirect pump (IDP)-QCL is its ability to overcome the 50% normalized population-inversion ( $\Delta n/n_{tot}$ ) limitation inherent to direct pump (DP)-QCLs. Figures 3(a) and 3(b) compare the spectrum of electron density in the optimized and reference design at  $T = 300\text{K}$ . Reduced thermal backfilling is mostly attributed to the reduced electron concentration in the injector, an inherent feature of IDP-QCLs. This effect is further enhanced by the large voltage defect ( $v_{def} > 130\text{meV}$ ) of this structure compared to the small  $v_{def} \sim 100\text{meV}$  of the reference structure (with a voltage efficiency of 52%). The 43% voltage efficiency of the proposed structure is comparable to 47% efficiency of a high performance triple resonant phonon QCL [17] despite the latter operates at a shorter wavelength. Another factor in temperature-insensitivity of QCLs is the carrier leakage into higher parasitic states. Thermal carrier leakage is proportional to  $\exp[-(\Delta E_{32} - \hbar\omega_{LO})/kT_{e2}]$ , where  $T_{e2}$  is the temperature of electrons in the state 2 [see Fig. 2] [20]. Both the reference and the optimized structures have  $\Delta E_{32} \sim 105\text{meV}$  and hence reduced thermal leakage due to resonant nature of the levels 3 and 2 with the pump frequency. Figure 4(a) depicts the spectrum of electron distribution in the reference design.

Obtaining a physical optical gain in the optimization process is essential, yet the other critical issue is the achievement of positive differential resistance (PDR) in the current density-filed characteristics. Otherwise, due to the electric field domain formation, the electric field distribu-

tion becomes inhomogeneous and the designed resonances do not form at each period. Resonant tunneling between coupled quantum wells, is often accompanied with a peak current when the subbands are aligned. This provides PDR, if the left subband is below the right one [21]. Levels  $e2'$  and  $i1$  play this significant role in the proposed structure. The relatively thin intra-injector barrier of 3.1 nm results in a large coupling strength of 3meV which in turn gives a peak current higher than the peak at 40kV/cm [see Fig. 4(b)].

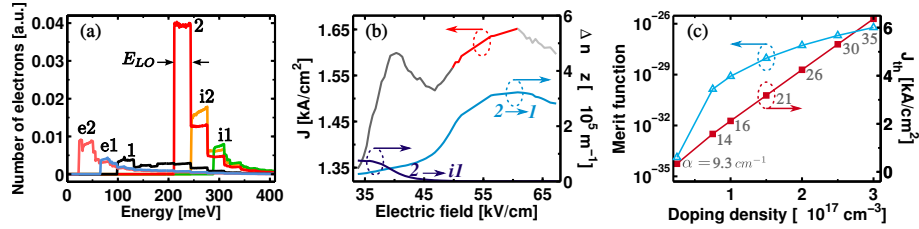


Fig. 4. (a) The spectrum of electrons distribution. (b) Current density-field characteristics of the optimized structure. At small electric fields, the transition  $2 \rightarrow i1$  lases with a wavelength similar to the transition  $2 \rightarrow 1$  at higher electric fields. The electron sheet density difference between these transitions multiplied by the corresponding dipole matrix element is shown. (c) The merit function and the threshold current density at room temperature as functions of the doping density. An effective optical loss ( $\alpha = (\alpha_m + \alpha_w)/\Gamma$ ) of  $35 \text{ cm}^{-1}$  is assumed for a doping density of  $3 \times 10^{17} \text{ cm}^{-3}$ . With the assumption of  $\Gamma = 0.65$ ,  $\alpha_m = 2 \text{ cm}^{-1}$ , and  $\alpha_w = \alpha_{\text{scat}} + \gamma n_{\text{dop}}$  [22], the optical loss at other doping concentrations can be extrapolated as shown in the figure.  $\gamma$  is a constant [22] and a value of  $\alpha_{\text{scat}} = 2.5 \text{ cm}^{-1}$  is assumed for the passive waveguide loss.

The doping density of the reference design is  $2.5 \times 10^{16} \text{ cm}^{-3}$  and it has a merit function of  $7.7 \times 10^{-36}$  at room temperature and  $9 \times 10^{-33}$  at 6K. The merit function for the optimized design at room temperature with same doping density is 17-fold larger. By increasing the electron density in the active mixing region of the optimized design to  $1.6 \times 10^{16} \text{ cm}^{-3}$  (corresponding the the doping  $7.5 \times 10^{16} \text{ cm}^{-3}$ ) five orders of magnitude increase of the merit function at room temperature, or 150-fold increase if compared with the reference design at 6K, can be achieved. Two orders of magnitude of this giant increase come directly from the increase of  $\chi^{(3)}(3\omega)$ . An additional contribution is due to increased pump power with higher doping level. Current density-field characteristics of the optimized structure is shown in Fig. 4(b). Figure 4(c) indicates the effect of the doping density on the merit function and the threshold current density. Apparently, the merit function increases significantly with the doping density but at the cost of increased threshold current density.

#### 4. Conclusion

In this work, a systematic optimization study of THG in QCLs is presented. Pathological structures corresponding to structures with unphysical electron coherence length are avoided with an appropriate physical condition. The optimization framework does not predefine injector barrier thickness. The optimized design shows a relatively high performance pump laser with large third-order susceptibility. Broad wavelength tunability with the electric field along with low threshold current density render this structure as an excellent wavelength converter.

#### Acknowledgment

This work has been partly supported by the Austrian Science Fund, contract F2514.